Journal of Advanced Ceramics
2024, **13**(11): 1835–1843
https://doi.org/10.26599/JAC.2024.9220980

Research Article

Effect of grain size on mechanical properties and tribological behavior of size-tunable high entropy diboride ceramics obtained by two-step SPS sintering

Yao Yang[1,2], Jianqiang Bi[1,2,✉], Linjing Qiao[1,2], Guandong Liang[1,2], Shuyong Liang[1,2], Shushuai Liu[1,2], Shaoyin Wang[1,2], Hongyu Gong[1,2], Zhao Qian[1,2], Jinwang Shi[3], Weiqiang Li[3]

[1] *Key Laboratory for Liquid–Solid Structural Evolution and Processing of Materials, Ministry of Education, Shandong University, Jinan 250061, China*
[2] *School of Materials Science and Engineering, Shandong University, Jinan 250061, China*
[3] *Shandong Huamei New Material Technology Co., Ltd., Weifang 261200, China*

Received: June 6, 2024; Revised: September 9, 2024; Accepted: September 27, 2024

© The Author(s) 2024. This is an open access article under the terms of the Creative Commons Attribution 4.0 International License (CC BY 4.0, http://creativecommons.org/licenses/by/4.0/).

Abstract: High-entropy diboride (HEB) ceramics constitute a novel class of ultrahigh-temperature ceramics that are appealing for applications in extreme environments. The relative density and grain size play important roles in tailoring the mechanical properties and wear resistance of HEBs, affecting their applications, such as high-temperature structural parts and thermal protection systems. In this study, highly dense (HfZrTaVNb)B_2 ceramics with size-tunable microstructures were successfully synthesized by spark plasma sintering combined with an ingenious two-step strategy. The effects of grain size on the mechanical properties and wear resistance of (HfZrTaVNb)B_2 ceramics were comprehensively investigated. The results indicated that the smaller grain size led to higher hardness and fracture toughness, and the relationship between hardness and grain size fitted the Hall–Petch equation well. In particular, the sample featuring a grain size of 1.64 μm and 97.6% density had the highest hardness and fracture toughness, 26.7 GPa and 4.6 MPa·$m^{1/2}$, respectively. Notably, it also demonstrated optimal wear resistance, displaying a minimal wear rate of only 2.53×10^{-6} $mm^3/(N\cdot m)$ under a 20 N load. Microstructure analysis revealed that the primary wear mechanism observed in (HfZrTaVNb)B_2 was oxidative wear under a 5 N load. Under a 10 N load, the wear mechanism comprised both oxidative and fracture wear. The wear mechanism became more complex and involved oxidation wear, fracture wear, abrasive wear, and fatigue wear at a 20 N load.

Keywords: high-entropy diborides (HEBs); two-step sintering; mechanical properties; tribology; microstructure regulation

1 Introduction

The transition metal diboride ceramics, such as hafnium diboride and zirconium diboride, exhibit excellent comprehensive properties, including high melting points, remarkable hardness, superior conductivity, corrosion resistance, wear resistance, and excellent thermal and chemical stability, indicating that they have significant applications in cutting tools and aerospace fields, such as nose caps and wing leading edge of hypersonic vehicles [1–5]. In recent years, the extension of material design concept of "high entropy" to ceramic materials has sparked significant research interest in high-entropy diboride (HEB) ceramics owing to their increased hardness and superior oxidation resistance. HEBs have become extremely promising candidates for high-temperature structural components and thermal protection systems [6–11].

However, owing to their strong covalent bonds and low diffusion coefficient, HEBs are difficult to densify, which significantly affects their mechanical properties and limits their application. For example, Yang *et al.* [12,13] utilized the spark plasma sintering (SPS) technique to fabricate the (HfZrTaVNb)B_2 ceramics at 1800 °C, resulting in a relative density of only 89%–94%, which was limited to 94.2% even at an elevated sintering temperature of 1900 °C. Consequently, researchers have implemented strategies such as introducing sintering aids and optimizing the preparation process to improve the sintering performance of HEBs. For example, Huang *et al.* [14] introduced metal Ni as a sintering aid in $(Hf_{0.2}Mo_{0.2}Ta_{0.2}Nb_{0.2}Ti_{0.2})B_2$ ceramics, sintering the sample with pressure-less sintering at 1800 °C. The addition of Ni resulted in highly dense HEBs; however, it also led to an abnormal increase in grain size, consequently deteriorating the mechanical properties. Feng *et al.* [15] fabricated $(Hf_{0.2}Zr_{0.2}Ti_{0.2}Ta_{0.2}Nb_{0.2})B_2$ ceramics via a two-step sintering process. Initially, the sample was maintained at 1650 °C for 5 min to eliminate residual oxides, followed by rapid heating to 2000–2200 °C for 10 min. Despite achieving a density of up to 99%, the grain size of the sample increased uncontrollably due to the second step of sintering at higher temperatures, thus decreasing the mechanical properties. Therefore, the prevailing challenge lies in the preparation of HEBs with highly dense and size-tunable grain structures.

It is well known that grain size plays an important role in regulating the mechanical properties and wear resistance of ceramics [16–18]. For example, Rezaie *et al.* [19] reported that the bending strength of ZrB_2–SiC composite ceramics decreased with increasing sizes of ZrB_2 grains and SiC grains. Moreover,

✉ Corresponding author.
E-mail: bjq1969@163.com

Zhou *et al.* [20] investigated the impact of grain size on the mechanical and wear properties of B_4C ceramics and revealed that a reduction in grain size can significantly enhance the hardness, fracture toughness, and wear resistance of B_4C ceramics. In addition, studies on the wear resistance of dual-phase high-entropy boride–carbide ceramics have demonstrated their outstanding wear resistance [21–23]. However, few studies have explored the wear characteristics of pure high-entropy diboride ceramics, and the effect of grain size on the mechanical properties of high-entropy diboride ceramics remains unclear.

To address the above problems, in this work, a series of highly dense (HfZrTaVNb)B_2 ceramics with adjustable grain sizes were synthesized by SPS technology combined with a facile two-step sintering strategy. The effects of grain size on the hardness, fracture toughness, and abrasive resistance of high-entropy (HfZrTaVNb)B_2 ceramics were investigated, and the underlying wear mechanism was revealed.

2 Experimental

The raw materials used for preparation of (HfZrTaVNb)B_2 ceramics include commercial powders of HfO_2 (99.9%, Macklin, China), ZrO_2 (99.0%, Macklin, China), Ta_2O_5 (99.5%, Macklin, China), V_2O_5 (99.99%, Macklin, China), Nb_2O_5 (99.9%, Macklin, China), B_4C (99.9%, 2–3 μm, Aladdin, China), and graphite (99.95%, Macklin, China). The boro/carbothermal reduction (BCTR) method was adopted to synthesize the HEB powder at 1600 °C, according to Eq. (1), with more details described in our previous study [24]. Briefly, the oxides were proportionally blended with B_4C and graphite powders manually in an agate mortar and then subjected to heating at 1600 °C for 2 h under an Ar flow in a tube furnace. To ensure the completion of the BCTR process and reduce the amount of residual oxides, excess 3 wt% B_4C and graphite powders were added. The added graphite powders can react with the byproduct B_2O_3 from the BCTR process to generate B_4C, facilitating the conversion of B_2O_3 to B_4C and thereby enhancing the BCTR reaction. Afterwards, the as-received HEB powders were loaded into a graphite mold with an inner diameter of 20 mm, lined with a layer of graphite foils around the internal surfaces of the mold and the top and bottom surfaces of the plungers to prevent adhesion. Each sample was sintered with 15.5 g of powder. Two-step sintering was carried out with an SPS apparatus (SPS-332HF, Fuji, Japan) under a uniaxial pressure of 30 MPa with a sintering atmosphere of Ar. The temperature was initially increased to 1200 °C at a rate of 100 °C/min, followed by a rise to 1750 °C at 55 °C/min, and it was maintained at 1750 °C for 12 min. Subsequently, the temperature was elevated to 1900 °C at a rate of 100 °C/min and held for 2, 5, 10, and 13 min, respectively. The obtained samples were named HEB2, HEB5, HEB10, and HEB13, as shown in Table 1. A grinding machine (ACC52SA1, Okamoto, Japan) was used to remove the carburized layer on the surface of the sintered samples for subsequent characterization.

$$2ZrO_2 + 2HfO_2 + Ta_2O_5 + V_2O_5 + Nb_2O_5 + \frac{53}{7}B_4C = 10\,(Hf_{0.2}Zr_{0.2}Ta_{0.2}V_{0.2}Nb_{0.2})\,B_2 + \frac{36}{7}B_2O_3 + \frac{53}{7}CO \quad (1)$$

An X-ray diffractometer (XRD; Rigaku Dmax-rc, Tokyo, Japan) was used to estimate the phase composition of the samples. A field-emission scanning electron microscope (FESEM; JSM-7800F, JEOL, Japan) equipped with an energy dispersive spectroscope (EDS; XMax-80, Oxford, UK) was used to identify the microstructures of samples. The electron backscatter diffraction (EBSD) measurements were conducted on an EBSD detector equipped with the JSM-7800F FESEM. The bulk densities of HEBs were determined via the Archimedes method with distilled water as the immersion medium. Vickers hardness testing of the samples was performed on a microhardness tester (HXD-1000TC, Shanghai Taiming Optical Instrument Co., Ltd., China) under a load of 9.8 N for a duration of 10 s. The fracture toughness (K_{IC}) was measured via the indentation technique with the same Vickers indenter at an applied load of 49 N according to Eq. (2) [25]:

$$K_{IC} = 0.16H\left(\frac{a}{c}\right)^{3/2}\sqrt{a} \quad (2)$$

where H is the hardness and a and c are the half diagonal of the indentation and the radial crack length, respectively. Each data point presented in this study represents the average of five independent tests.

The wear resistance of each sample was investigated by using a friction and wear testing machine (GF-I, Lanzhou Zhongke Kaihua Technology Development Co., Ltd., China) under dry sliding conditions. The sample surface was finely polished. As shown in Fig. 1, the tribological partner was a highly polished Si_3N_4 ball with a diameter of 6 mm, and the wear test was carried out at 5, 10, and 20 N; the reciprocating length was 5 mm, and the sliding time was 60 min. The wear scar profile was collected by a laser confocal scanning microscope (LSM800, Zeiss, Germany). The specific wear rates were then calculated according to Eq. (3):

$$W = \frac{V}{dL} \quad (3)$$

where W is the specific wear rate; V is the volume loss; d is the sliding distance; and L is the applied load.

3 Results and discussion

3.1 Microstructures of HEBs

Table 1 lists the relative densities of (HfZrTaVNb)B_2 samples obtained by two-step sintering with different holding time, i.e., HEB2, HEB5, HEB10, and HEB13, with 97.6%, 97.5%, 97.0%, and 97.3%, respectively. This finding indicates that dense structures in the HEBs were achieved via the two-step sintering strategy. According to Ref. [13], significant intracrystalline pores exist in the SPS-ed (HfZrTaVNb)B_2 ceramics. This occurred because the rapid heating rate during the SPS process led to a sudden rise in temperature associated with unexpected fast grain growth, rendering that the grain boundary migration rate exceeds that of

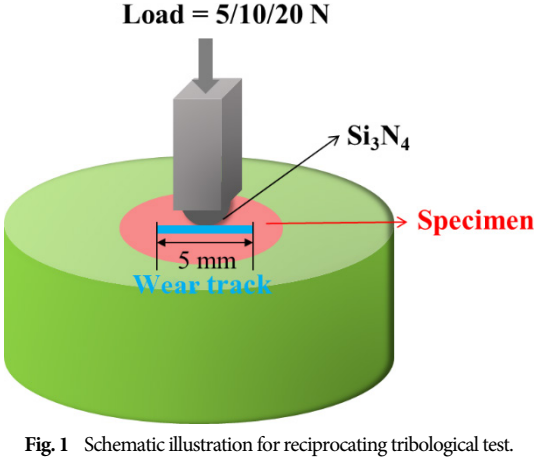


Fig. 1 Schematic illustration for reciprocating tribological test.

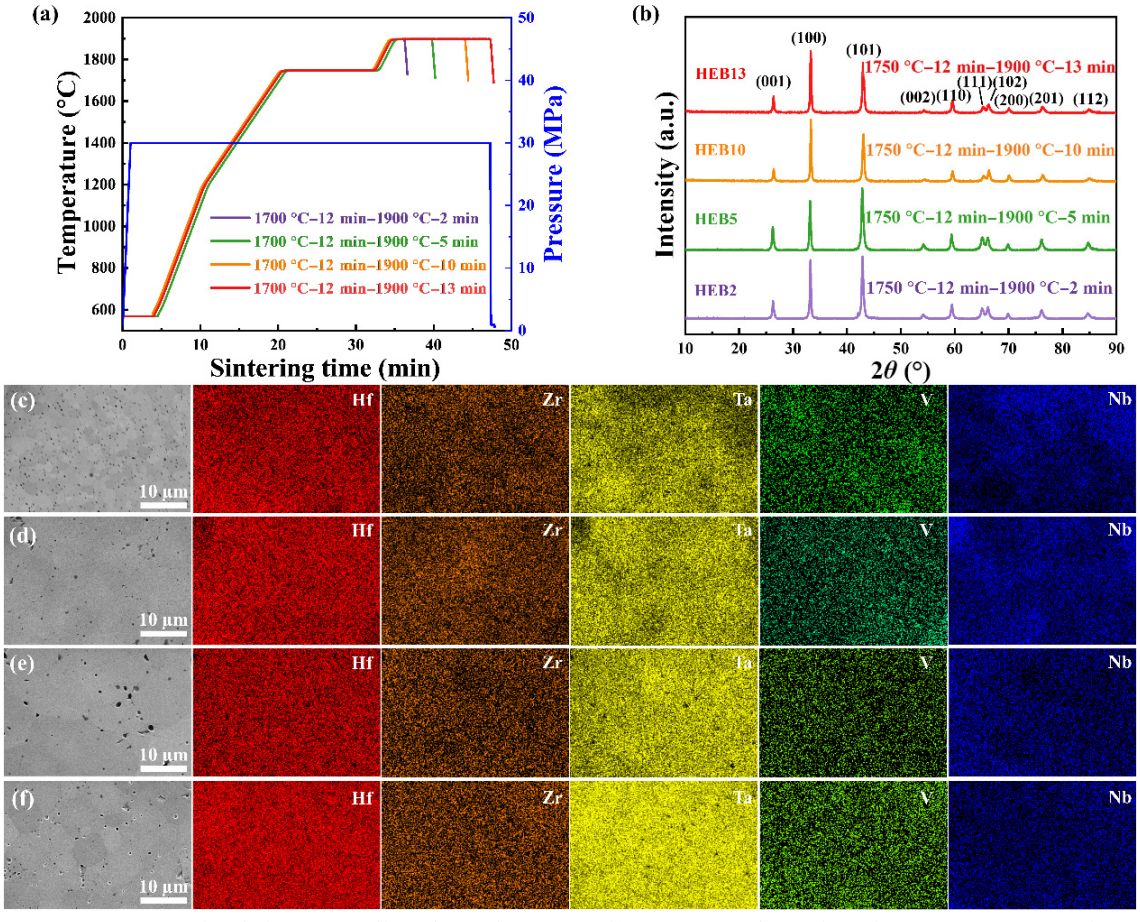


Fig. 2 (a) Sintering temperature and applied pressure profile used to synthesize HEBs. (b) XRD patterns of as-synthesized HEB2, HEB5, HEB10, and HEB13 samples. EDS elemental mapping of polished surfaces of HEB ceramics: (c) HEB2, (d) HEB5, (e) HEB10, and (f) HEB13.

Table 1 Summary of sample name, relative density, and grain size of $(HfZrTaVNb)B_2$ ceramics sintered under different conditions

Sample name	Composition	Sintering conditions	Relative density (%)	Grain size (μm)
HEB2	$(HfZrTaVNb)B_2$	1750 °C/12 min–1900 °C/2 min	97.6	1.64
HEB5	$(HfZrTaVNb)B_2$	1750 °C/12 min–1900 °C/5 min	97.5	5.21
HEB10	$(HfZrTaVNb)B_2$	1750 °C/12 min–1900 °C/10 min	97.0	7.34
HEB13	$(HfZrTaVNb)B_2$	1750 °C/12 min–1900 °C/13 min	97.3	8.53
HEB	$(HfZrTaVNb)B_2$	1900 °C/2 min	93.8	1.25

pore migration [26,27]. Once intracrystalline pores are formed, they cannot be eliminated by increasing the sintering temperature, resulting in a decrease in the relative density of the sintered ceramics [28]. Therefore, the heating rate ranged from 1200 to 1750 °C, and the sample was held at a lower temperature of 1750 °C for a long time, as shown in Fig. 2(a), which was conducive to reducing the number of intracrystalline pores and thus increasing the relative density of high-entropy diboride ceramics. The selection of 1750 °C was based on our pre-experimental results, as shown in Fig. 3, which shows that the $(HfZrTaVNb)B_2$ ceramic exhibits a continual densification process, while the grain size remains almost unchanged with the extension of holding time during sintering when the sintering temperature is in the range of 1700–1800 °C. As a comparison, without the first step of holding at 1750 °C and the slowing down of the heating rate, the relative density of the $(HfZrTaVNb)B_2$ ceramics obtained by direct rapid heating to 1900 °C for 2 min is merely 93.8%, validating the conclusion. Figure 2(b) presents the XRD patterns for the as-synthesized HEBs, showing that all the samples possessed the typical hexagonal AlB_2 structure without other detected impurities, confirming the successful fabrication of $(HfZrTaVNb)B_2$ samples. In the case of sample HEB2, a faint peak appeared at the left side of the diffraction peak corresponding to the (101) plane, which was attributed to the presence of trace amounts of unsolved secondary boride phase. The weak peak gradually diminished with increasing holding time, suggesting the occurrence of diffusion and solid-solution processes at high temperatures. EDS mapping analysis of the HEB samples was performed, and the results are shown in Figs. 2(c)–2(f). The transition metal elements displayed a uniform distribution, confirming the formation of single-phase high-entropy ceramics. There was slight segregation of Nb and Ta in HEB2 and HEB5, which was attributed to the short holding time and slow diffusion kinetics, as reported in Refs. [5,29]. However, with increasing holding time, all the elements exhibited a more homogeneous distribution, which is in agreement with the XRD results. Moreover, there is little difference in the relative densities of HEB2, HEB5, HEB10, and HEB13 samples, revealing that the sintering time of the second step has almost no effect on the relative density of samples.

清華大学出版社 Tsinghua University Press | SciOpen

Figure 4 displays the inverse pole figure (IPF) diagram and grain size distribution of samples HEB2, HEB5, HEB10, and HEB13 via EBSD analysis. The grain size of the samples increased from 1.64 μm for HEB2 to 8.53 μm for HEB13 as the holding time of the second step gradually increased from 2 to 13 min. These findings suggest that the grain structure of the (HfZrTaVNb)B_2 ceramics grew rapidly at 1900 °C. Figure 5 shows SEM images of the polished surfaces in backscattered electron (BSE) mode and the fracture surfaces of the as-synthesized samples, revealing that the grain sizes of HEB2, HEB5, HEB10, and HEB13 increase gradually, which is in agreement with Fig. 4. Notably, there is a small amount of black phase in addition to the HEB phase in Figs. 5(a)–5(d), which should be residual B_4C [12]. The residual B_4C grains also grew gradually with prolonging the second-step sintering time. In addition, some microcracking can be found on the polished surfaces of samples HEB5, HEB10, and HEB13 by close observation, which can be attributed to the mismatch in thermal expansion coefficients between B_4C and the high-entropy diborides [30] and the anisotropic thermal expansion of high-entropy diboride ceramics [5]. The spark plasma sintering technique utilized in this study is known for its extremely rapid cooling speed after the sintering process. Consequently, the sample experiences stress during the quick cooling process due to the mismatch of thermal expansion coefficients, leading to the formation of microcracking. Notably, no obvious microcracking was observed in sample HEB2, which was likely attributed to its refined grain size. On one hand, the refinement of grains led to a significant increase in the strength of the sample through the refinement strengthening effect, which helps to resist stress and prevent microcracking. On the other hand, grain refinement means a higher grain boundary density, facilitating the dissipation of stress, further preventing the formation of microcracking. SEM images of the fracture surface for the samples in Figs. 5(e)–5(h) reveal that the fracture mode of (HfZrTaVNb)B_2 ceramics features transgranular fracture, and there are only a few pores except for B_4C, which proves the successful preparation of highly dense high-entropy diboride ceramics.

3.2 Mechanical properties of HEBs

Figure 6 depicts the relationship between the hardness and grain size of the samples. The hardness of the (HfZrTaVNb)B_2 ceramics clearly increases with the decrease in grain size. Specifically, HEB2, with a minimum grain size of 1.64 μm, has the highest hardness, reaching 26.7 GPa. The Hall–Petch equation given in Eq. (4) expresses the relationship between the hardness and grain size of polycrystalline ceramic materials [31]:

$$H = H_0 + kd^{-1/2} \tag{4}$$

where H is the hardness of ceramics; H_0 represents the intrinsic hardness of samples; k is the Hall-Petch constant, representing the degree of grain refinement that contributes to the hardness,

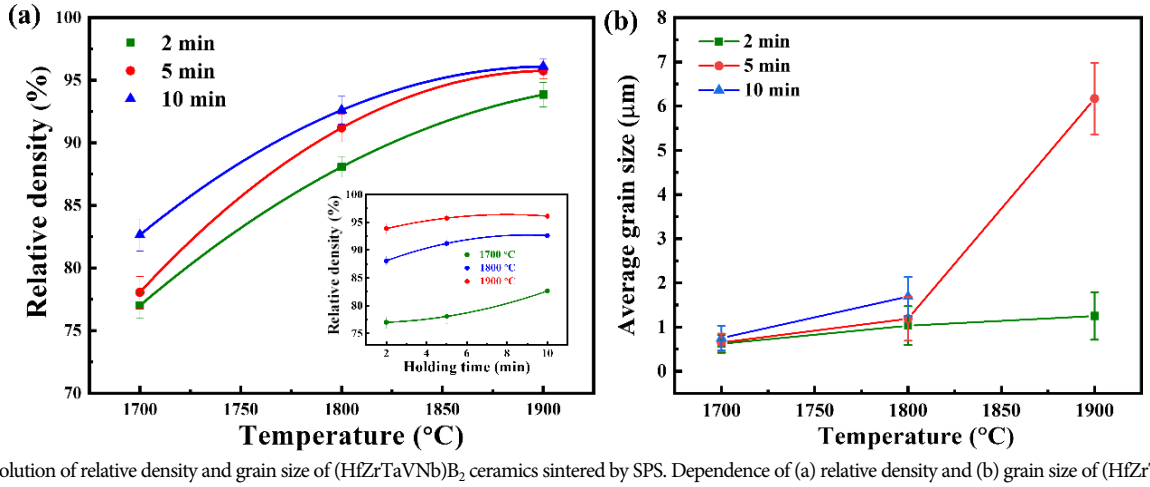


Fig. 3 Evolution of relative density and grain size of (HfZrTaVNb)B_2 ceramics sintered by SPS. Dependence of (a) relative density and (b) grain size of (HfZrTaVNb)B_2 ceramics on sintering temperature and sintering time.

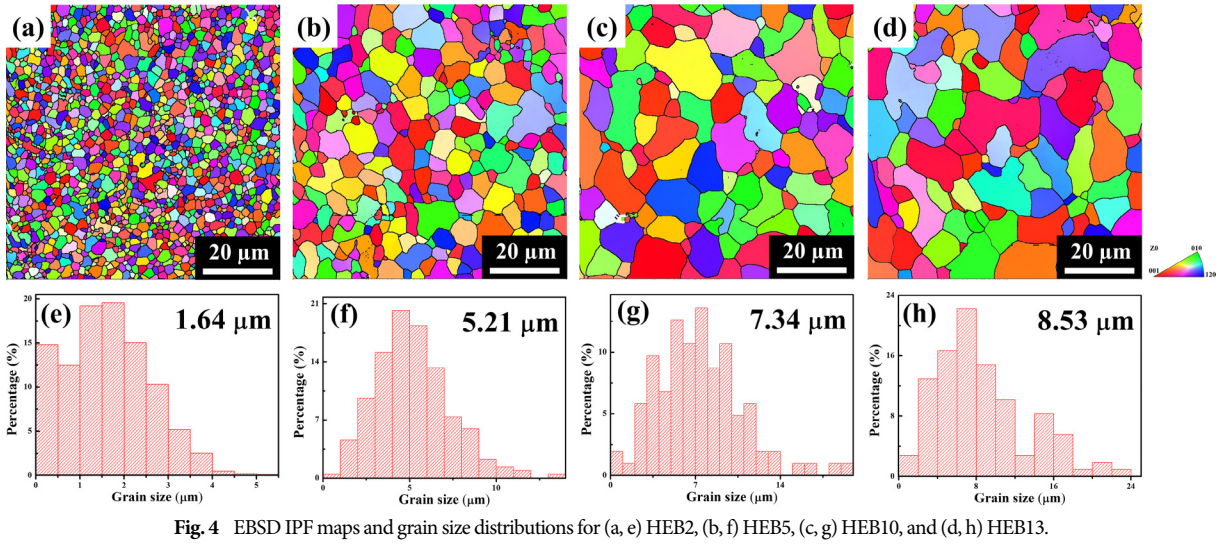


Fig. 4 EBSD IPF maps and grain size distributions for (a, e) HEB2, (b, f) HEB5, (c, g) HEB10, and (d, h) HEB13.

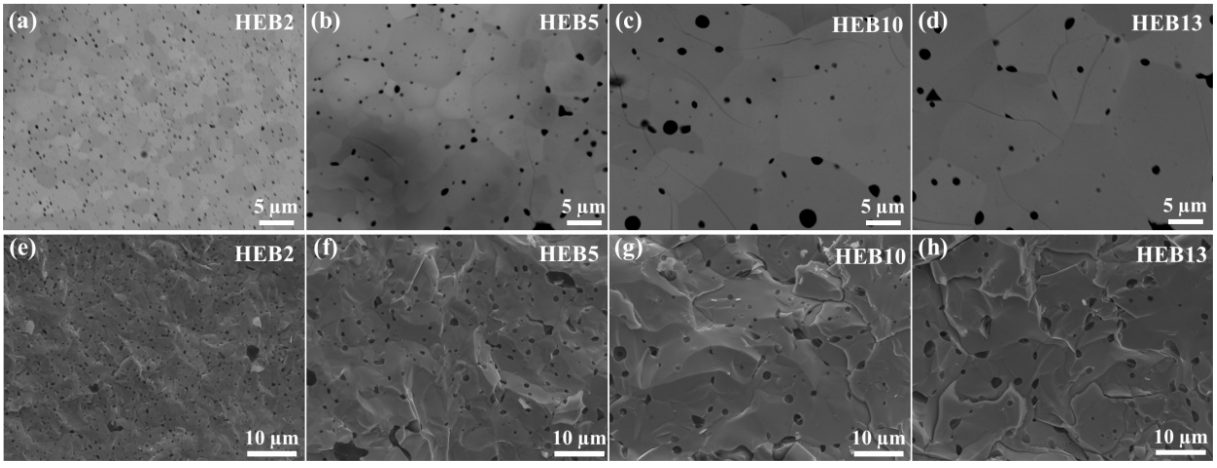


Fig. 5 SEM images of (a–d) polished surfaces under BSE modes and (e–h) fracture surfaces under secondary electron modes for samples.

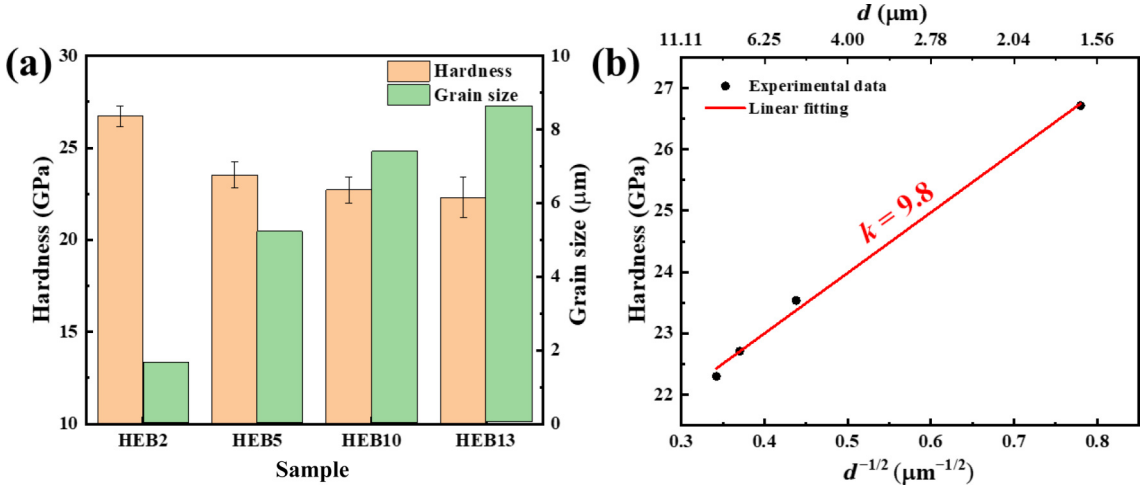


Fig. 6 (a) Hardness and grain size of HEB samples and (b) hardness of HEB samples as a function of inverse square root of grain size.

and d is the grain size of ceramics. The relationships between the hardness and the inverse square root of grain size of HEB2, HEB5, HEB10, and HEB13 samples were plotted according to Eq. (3) and depicted in Fig. 6(b), exhibiting excellent linear fitting and yielding a Hall–Petch coefficient (k) of 9.8 based on the fitting results. These results indicate that the as-synthesized HEBs in this study possess a sufficiently dense structure and that grain size refinement greatly contributes to increasing the hardness of HEBs [32].

Figure 7(a) displays the fracture toughness and grain size of the samples. Similarly, the fracture toughness of (HfZrTaVNb)B_2 ceramics tends to increase as the grain size decreases. Specifically, with the smallest grain size of 1.64 μm, HEB2 had the highest fracture toughness of 4.6 MPa·m$^{1/2}$. This finding indicates that the refinement of the microstructure contributes to the improvement of fracture toughness of HEBs. However, the differences in fracture toughness values among the samples were slight, possibly because the fracture toughness of samples depended not only on the grain size but also on other factors, such as microcracking. As mentioned above, microcracking was observed in samples HEB5, HEB10, and HEB13. It is well known that toughening by microcracks has been rigorously verified [33], and the effect of microcracking on the fracture toughness of HEBs needs to be investigated in future research. Figure 7(b) displays the SEM image of the indentation sites for the HEB2 sample tested at 5.0 kg for fracture toughness assessment, with the lengths of the cracks and indentations clearly labeled. The locally enlarged crack is shown in Fig. 7(c), suggesting crack deflection and branching, which contribute to the high fracture toughness.

3.3 Tribological properties of HEBs

To characterize the wear resistance of the as-synthesized HEBs, Fig. 8 depicts the coefficient values of friction and the calculated average specific wear rates of the investigated samples of HEB2, HEB5, HEB10 and HEB13 at 20 N load. Figure 8(a) shows that the coefficients of friction for all the samples increased sharply in the initial stage and fluctuated greatly, with a steady state subsequently attained; a similar phenomenon has been reported by Murthy *et al.* [34]. For all the samples, the coefficients of friction eventually stabilized at approximately 0.6, which aligns with the values reported for single diborides and dual-phase high-entropy ceramics in Refs. [23,34–36]. The small difference in coefficients of friction for all the samples demonstrates that the influence of the grain size on the coefficients of friction for the samples is negligible. Figure 8(b) shows the typical cross-sectional profiles extracted from the wear track of all the samples after sliding at 20 N load, exhibiting that the width of the wear tracks for HEB2 is the narrowest and that the depth of the wear tracks for HEB10 is the deepest. Figure 8(c) presents the average specific wear rates for all samples calculated from Fig. 8(b), with 2.53×10^{-6}, 3.47×10^{-6}, 1.10×10^{-5}, and 4.61×10^{-6} mm^3/(N·m) for HEB2, HEB5, HEB10, and HEB13, respectively, indicating the excellent wear resistance of HEBs. In general, the HEB samples with smaller grain sizes have a lower wear rate, i.e., better wear resistance,

清華大学出版社 Tsinghua University Press | SciOpen

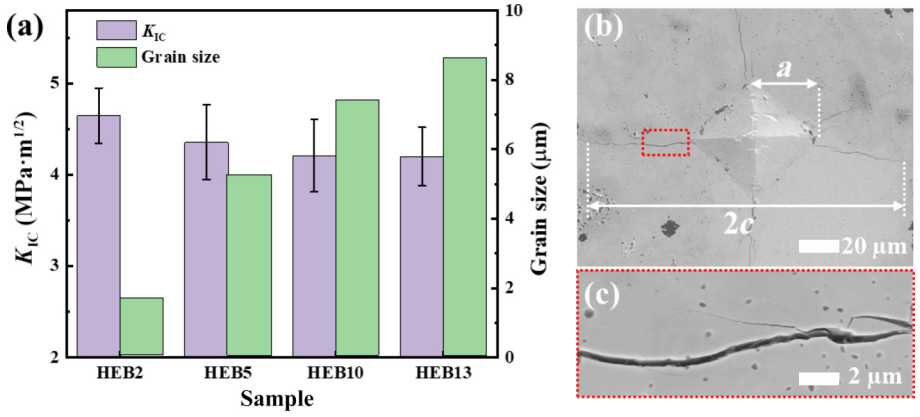


Fig. 7 (a) Fracture toughness and grain size of HEB samples. SEM images of (b) indentation site of HEB2 sample tested at 5.0 kg and (c) a locally enlarged crack in (b).

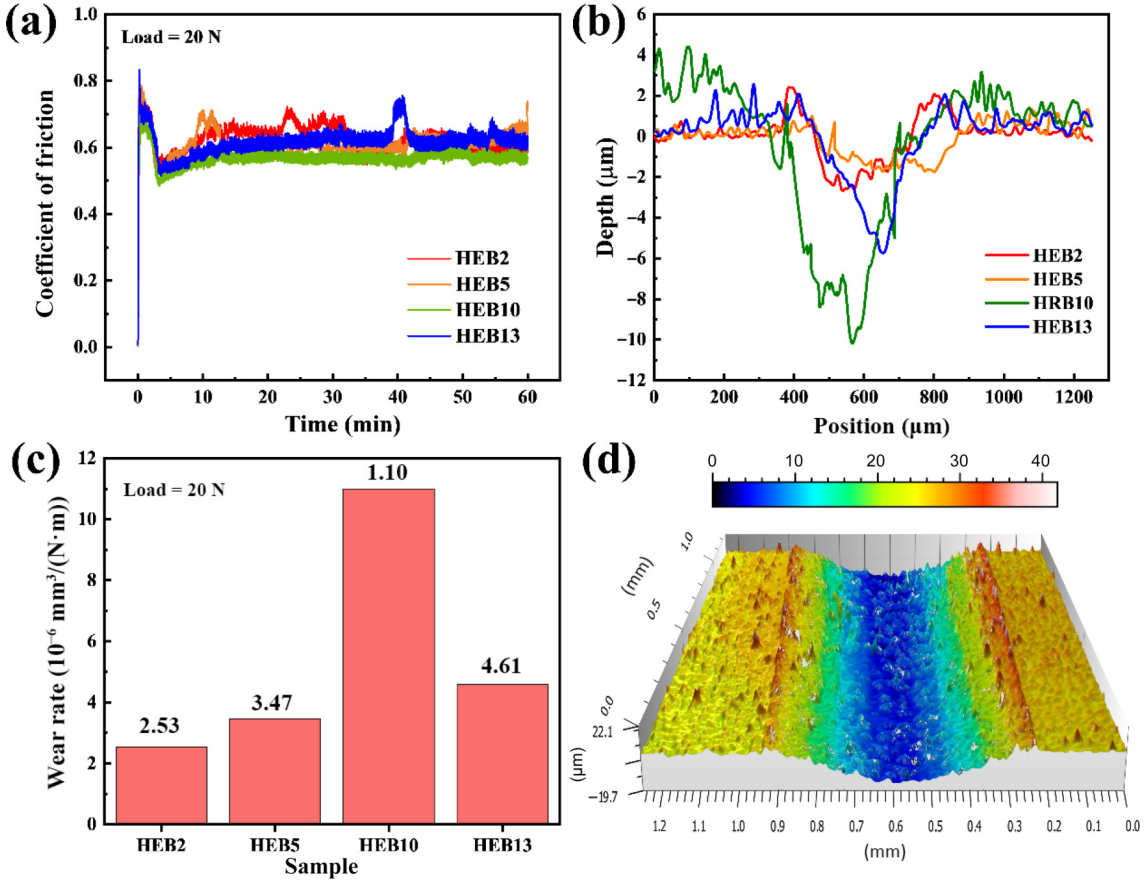


Fig. 8 Effect of grain size on wear resistance of HEBs. (a) Measured coefficient of friction, (b) typical cross section profiles extracted from the wear track, and (c) calculated wear rate of HEB samples under 20 N load. (d) Optical 3D profile images of wear tracks of HEB10 under 20 N load.

because the mechanical properties of the materials, especially hardness and fracture toughness, influence their wear behavior [37]. The effects of hardness and fracture toughness on the wear rate of materials can be described by Eq. (5) [20]:

$$W \propto \frac{P^{1/8}}{K_{Ic}^{1/2} H^{5/8}} \left(\frac{E}{H}\right)^{4/5} \quad (5)$$

where W is the wear rate; P is the applied load; K_{IC} is the fracture toughness; H is the hardness; and E represents the elastic modulus. According to Eq. (5), there is an inverse relationship of the hardness and fracture toughness of the material with its wear rate. From Figs. 6 and 7, we can conclude that an increase in the grain size of a sample leads to a decrease in its mechanical properties, consequently resulting in an elevated wear rate. However, HEB10 exhibits a higher wear rate than HEB13, possibly because the slight difference in grain size between HEB10 and HEB13 leads to little variation in their mechanical properties. Hence, the influence of the relative density on the wear rate is highlighted. The relative density of sample HEB10 is relatively low, accounting for its higher wear rate. The optical three-dimensional (3D) profile image of the wear tracks for HEB10 under a 20 N load in Fig. 8(d) shows that the center of the wear tracks is the deepest, indicating that the center has been worn the most.

To further investigate the effect of the applied load on the friction behavior of HEBs, the worn cross section and calculated average specific wear rates of HEB2 tested under different loads for 1 h are illustrated in Fig. 9. Figure 9 shows that the wear rates

of HEB2 under 5, 10, and 20 N loads are 3.40×10^{-6}, 4.11×10^{-6}, and 2.53×10^{-6} mm^3/(N·m), respectively. Recently, Rodríguez-Rojas *et al.* [38] prepared an ultrahard B_4C–SiC–TiB_2 composite, which exhibited a high hardness of 35 GPa and a fracture toughness of 4.1 MPa·m$^{1/2}$. When a Si_3N_4 ball was used as the friction pair, the wear rate of the B_4C–SiC–TiB_2 composite under a 20 N load was reported to be 3.1×10^{-6} mm^3/(N·m). This proves the superiority of high-entropy ceramics. Furthermore, the HEB samples in the present study also exhibited better wear resistance than some other single-metal diboride ceramics and their composites reported previously [39–41].

The microstructures of the worn surfaces of HEB2 under different loads were analyzed to elucidate the underlying wear mechanism. Figure 10 gives the microscopic analysis of worn surface of HEB2 samples under a 5 N load. Figure 10(a) shows that there is no noticeable damage to the wear surface, with a width of wear crack only 490 μm, similar to the results reported by Zhang *et al.* [42] for high-entropy ceramics of $(Dy_{0.2}Ho_{0.2}Er_{0.2}Tm_{0.2}Lu_{0.2})B_{12}$. As shown in Fig. 10(b), area B inside the wear track in Fig. 10(a) has a relatively clean surface with no traces of debris or cracks. The corresponding elemental distribution analysis reveals the presence of oxygen on the worn surface, indicating that the oxidative wear caused by friction-generated heat predominantly governs the wear mechanism of the HEB2 sample under the load of 5 N.

Figure 11 presents a typical morphology of the wear track of HEB2 under a 10 N load, where pits can be clearly observed in the track center, suggesting a wear form of pitting corrosion. Expanding the middle region B in Fig. 11(a), as shown in Fig. 11(b), illustrates a clear fracture on the worn surface. Further analysis of region C in Fig. 11(b) reveals that some diboride grains have been completely oxidized, as shown in Fig. 11(c). The element distribution in grain 1 is predominantly oxygen, while that in grain 2 is primarily boron. In this case, the wear mechanism of the HEB2 sample encompasses both fracture and oxidation wear.

Figure 12 displays the worn surface morphology of sample HEB2 under a 20 N load. Figure 12(a) clearly shows that more significant wear has occurred on the sample surface, with wider wear tracks of approximately 539 μm. The corresponding EDS spectra indicate high presence of O element in the wear tracks, indicating severe oxidation under reciprocating friction. The black phase with enriched B element signifies residual boron carbide, while the absence of N element enrichment within the wear track indicates no element transfer during the reciprocating friction process. Figures 12(a) and 12(b) show that obvious changes have taken place on the surface of the wear track. The surface is relatively rough, with distinct cracks and large pits, and a certain degree of layered spalling damage occurs, which are typical characteristics of abrasive wear and fatigue wear [42,43]. Therefore, the wear mechanism of HEB2 samples under 20 N

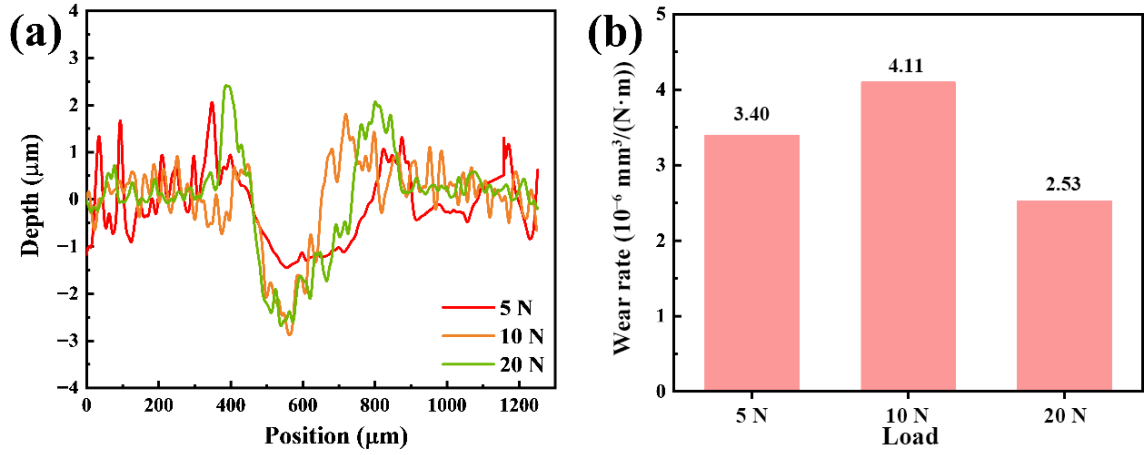


Fig. 9 Effect of applied load on wear resistance of HEBs: (a) typical cross section profiles extracted from wear track and (b) calculated wear rates of HEB samples under 5, 10, and 20 N loads.

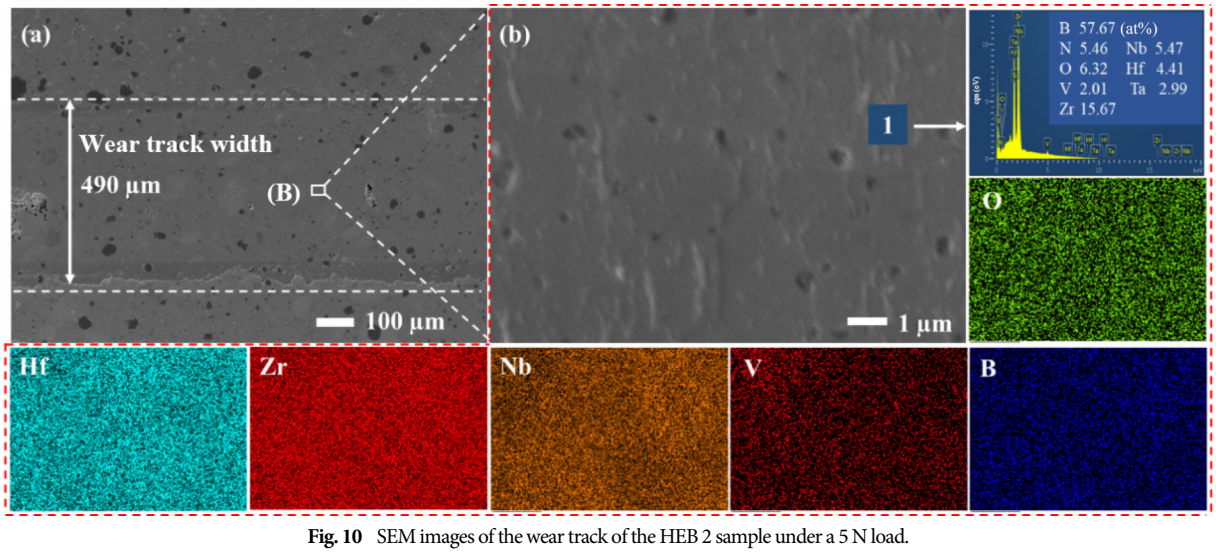


Fig. 10 SEM images of the wear track of the HEB 2 sample under a 5 N load.

清華大学出版社 Tsinghua University Press | SciOpen

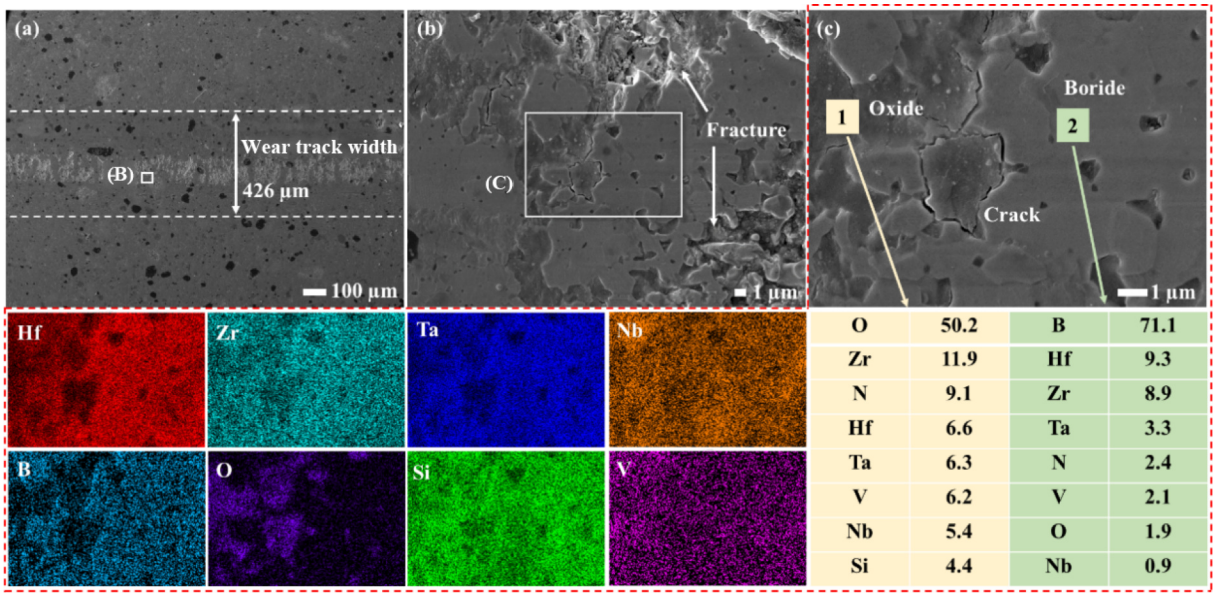


Fig. 11 SEM images of wear track of HEB2 sample under 10 N load.

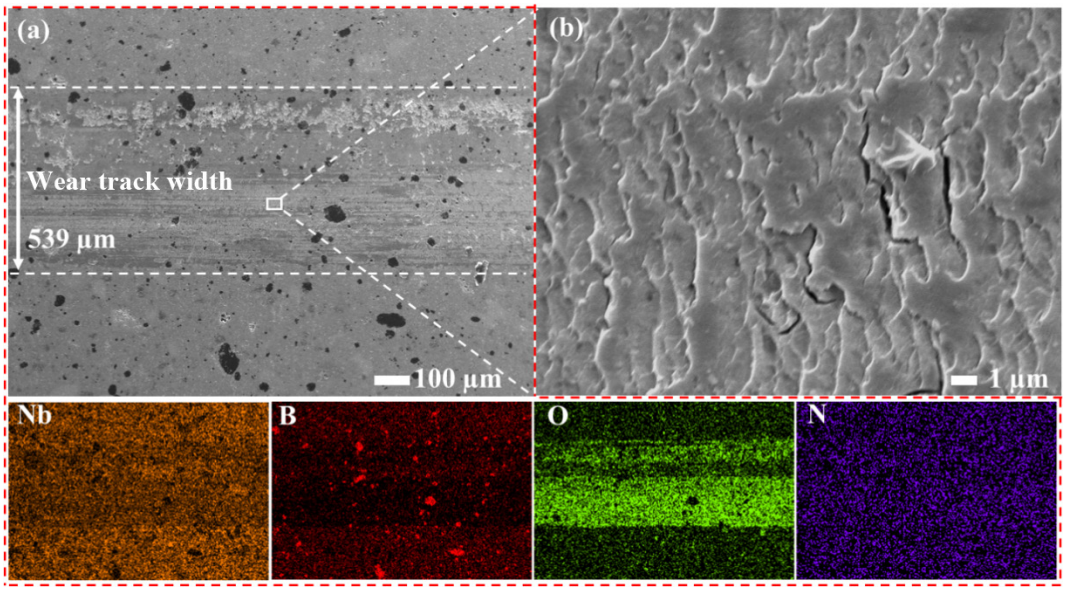


Fig. 12 SEM images of wear track of HEB2 sample under 20 N load.

load is complicatedincluding fracture wear, oxidation wear, abrasive wear, and fatigue wear.

4 Conclusions

In summary, high-entropy diboride powders were synthesized by the boro/carbonothermal reduction method in this study, followed by two-step spark plasma sintering, resulting in highly dense (HfZrTaVNb)B_2 high-entropy diboride ceramics with regulable grain sizes. Furthermore, the influences of grain size on the mechanical properties and friction and wear properties of high-entropy diboride ceramics were investigated, and the following conclusions were drawn:

1) The influence of the sintering time of the second step on the relative density of samples was negligible but the effect on the grain size was great. When the second-step holding time was 2, 5, 10, and 13 min, the relative densities of the samples were 97.6%, 97.5%, 97.0%, and 97.3%, and their grain sizes were 1.64, 5.21, 7.34, and 8.53 μm, respectively.

2) The hardness and fracture toughness of (HfZrTaVNb)B_2 high-entropy diboride ceramics increased with decreasing grain size, and the hardness and grain size were in accordance with the Hall–Petch relationship. The highest values were achieved for the sample with an average grain size of 1.64 μm, 26.7 GPa, and 4.6 MPa·$m^{1/2}$, respectively.

3) The grain refinement in the (HfZrTaVNb)B_2 high-entropy diboride ceramics resulted in a notable improvement in wear resistance. Specifically, at a load of 20 N, the sample exhibited the lowest wear rate when the grain size was 1.64 μm, which was only 2.53×10^{-6} mm^3/(N·m). Under varying applied loads, (HfZrTaVNb)B_2 exhibited distinct wear behaviors: oxidation wear predominated at 5 N; a combination of oxidation wear and fracture wear was evident at 10 N; and oxidation wear, fracture wear, abrasive wear, and fatigue wear were all observed at 20 N.

Acknowledgements

This work was supported by the Key R&D Program of Shandong Province, China (2023CXGC010305) .

Declaration of competing interest

The authors have no competing interests to declare that are relevant to the content of this article.

References

[1] Silvestroni L, Gilli N, Sangiorgi A, *et al.* Multi-phase (Zr,Ti,Cr)B_2 solid solutions: Preparation, multi-scale microstructure, and local properties. *J Adv Ceram* 2023, **12**: 414–431.

[2] Zhu QQ, Ji W, Zou J, *et al.* Strengthening $Hf_{0.95}Ta_{0.05}B_2$ ceramic with ultrafine grains and high-density dislocations. *J Eur Ceram Soc* 2023, **43**: 6599–6605.

[3] Zhou YZ, Zhu QQ, Xu L, *et al.* Effects of group-VB transition metals diborides substitution on HfB_2-based ceramics. *J Eur Ceram Soc* 2023, **43**: 739–747.

[4] Bajpai S, Bhadauria A, Venkateswaran T, *et al.* Spark plasma joining of HfB_2–ZrB_2 based ultra high temperature ceramics using Ni interlayer. *Mater Sci Eng A* 2022, **838**: 142818.

[5] Monteverde F, Saraga F, Gaboardi M, *et al.* Compositional pathways and anisotropic thermal expansion of high-entropy transition metal diborides. *J Eur Ceram Soc* 2021, **41**: 6255–6266.

[6] Liu JX, Shen XQ, Wu Y, *et al.* Mechanical properties of hot-pressed high-entropy diboride-based ceramics. *J Adv Ceram* 2020, **9**: 503–510.

[7] Zhang WM, Dai FZ, Xiang HM, *et al.* Enabling highly efficient and broadband electromagnetic wave absorption by tuning impedance match in high-entropy transition metal diborides (HE TMB_2). *J Adv Ceram* 2021, **10**: 1299–1316.

[8] Zhang Y, Sun SK, Guo WM, *et al.* Optimal preparation of high-entropy boride-silicon carbide ceramics. *J Adv Ceram* 2021, **10**: 173–180.

[9] Gild J, Zhang YY, Harrington T, *et al.* High-entropy metal diborides: A new class of high-entropy materials and a new type of ultrahigh temperature ceramics. *Sci Rep* 2016, **6**: 37946.

[10] Qiao LJ, Liu Y, Gao Y, *et al.* First-principles prediction, fabrication and characterization of $(Hf_{0.2}Nb_{0.2}Ta_{0.2}Ti_{0.2}Zr_{0.2})B_2$ high-entropy borides. *Ceram Int* 2022, **48**: 17234–17245.

[11] Yang Y, Bi JQ, Gao XC, *et al.* Facile synthesis of nanocrystalline high-entropy diboride powders by a simple Sol-gel method and their performance in supercapacitor. *Ceram Int* 2023, **49**: 19523–19527.

[12] Yang Y, Bi JQ, Sun KN, *et al.* Novel $(Hf_{0.2}Zr_{0.2}Ta_{0.2}V_{0.2}Nb_{0.2})B_2$ high entropy diborides with superb hardness sintered by SPS under a mild condition. *Ceram Int* 2022, **48**: 30859–30867.

[13] Yang Y, Bi JQ, Sun KN, *et al.* The effect of chemical element on hardness in high-entropy transition metal diboride ceramics. *J Eur Ceram Soc* 2023, **43**: 5774–5781.

[14] Huang ZJ, Su LF, Xu L, *et al.* Dense $(Hf_{0.2}Mo_{0.2}Ta_{0.2}Nb_{0.2}Ti_{0.2})B_2$ ceramics prepared by pressureless sintering with Ni additives. *Ceram Int* 2023, **49**: 27651–27656.

[15] Feng L, Fahrenholtz WG, Hilmas GE. Processing of dense high-entropy boride ceramics. *J Eur Ceram Soc* 2020, **40**: 3815–3823.

[16] El-Awady JA. Unravelling the physics of size-dependent dislocation-mediated plasticity. *Nat Commun* 2015, **6**: 5926.

[17] Moshtaghioun BM, Gomez-Garcia D, Dominguez-Rodriguez A, *et al.* Grain size dependence of hardness and fracture toughness in pure near fully-dense boron carbide ceramics. *J Eur Ceram Soc* 2016, **36**: 1829–1834.

[18] Zou Q, Yuan ZX, Li YG, *et al.* Synthesis and characterization of onion-like carbon/$TiN_{0.3}$ enhanced Si_3N_4 composites. *Mater Sci Eng A* 2024, **897**: 146266.

[19] Rezaie A, Fahrenholtz WG, Hilmas GE. Effect of hot pressing time and temperature on the microstructure and mechanical properties of ZrB_2–SiC. *J Mater Sci* 2007, **42**: 2735–2744.

[20] Zhou ZH, Xia J, Wang MB, *et al.* Effect of grain size on tribological behavior of hot-pressed boron carbide sliding against alumina balls. *Int J Appl Ceram Technol* 2024, **21**: 2136–2150.

[21] Naughton-Duszová A, Medveď D, Ďaková L, *et al.* Dual-phase high-entropy carbide/boride ceramics with excellent tribological properties. *J Eur Ceram Soc* 2024, **44**: 5391–5400.

[22] Naughton-Duszová A, Medveď D, Ďaková L, *et al.* Wear characteristics of dual-phase high-entropy ceramics: Influence of the testing method. *Int J Appl Ceram Technol* 2024, **21**: 2678–2689.

[23] Naughton-Duszová A, Medveď D, Ďaková L, *et al.* Highly wear resistant dual-phase (Ti–Zr–Nb–Hf–Ta)C/(Ti–Zr–Nb–Hf–Ta)B_2 high-entropy ceramics. *Adv Appl Ceram* 2023, **122**: 107–118.

[24] Yang Y, Bi JQ, Sun KN, *et al.* Toughened bulk high-entropy diborides with high hardness and enhanced oxidation resistance *via* SiC whiskers. *Mater Charact* 2024, **210**: 113814.

[25] Evans AG, Charles EA. Fracture toughness determinations by indentation. *J Am Ceram Soc* 1976, **59**: 371–372.

[26] Yang TT, Li Y, Wu WW, *et al.* The synergistic effect of dual substitution of Al and Sb on structure and ionic conductivity of $Li_7La_3Zr_2O_{12}$ ceramic. *Ceram Int* 2018, **44**: 1538–1544.

[27] Xu HY, Ji W, Guo WM, *et al.* Enhanced mechanical properties and oxidation resistance of zirconium diboride ceramics *via* grain-refining and dislocation regulation. *Adv Sci* 2022, **9**: 2104532.

[28] Huang ZY, Shi Y, Zhang YT, *et al.* An effective strategy for preparing transparent ceramics using nanorod powders based on pressure-assisted particle fracture and rearrangement. *J Adv Ceram* 2022, **11**: 1976–1987.

[29] Feng L, Fahrenholtz WG, Hilmas GE, *et al.* Effect of Nb content on the phase composition, densification, microstructure, and mechanical properties of high-entropy boride ceramics. *J Eur Ceram Soc* 2021, **41**: 92–100.

[30] Sigl LS, Kleebe HJ. Microcracking in B_4C–TiB_2 composites. *J Am Ceram Soc* 1995, **78**: 2374–2380.

[31] Hall EO. The deformation and ageing of mild steel: III discussion of results. *Proc Phys Soc B* 1951, **64**: 747–753.

[32] Dong WG, Xin SW, Ding SJ, *et al.* Dense nanocrystalline ReB_2 bulk with ultrahigh hardness. *Mater Sci Eng A* 2023, **885**: 145635.

[33] Lee SG, Kim YW, Mitomo M. Relationship between microstructure and fracture toughness of toughened silicon carbide ceramics. *J Am Ceram Soc* 2001, **84**: 1347–1353.

[34] Murthy TSRC, Basu B, Srivastava A, *et al.* Tribological properties of TiB_2 and TiB_2–$MoSi_2$ ceramic composites. *J Eur Ceram Soc* 2006, **26**: 1293–1300.

[35] Medveď D, Balko J, Sedlák R, *et al.* Wear resistance of ZrB_2 based ceramic composites. *Int J Refract Met Hard Mater* 2019, **81**: 214–224.

[36] Mor M, Meiser M, Langhof N, *et al.* Tribological behavior of carbon fiber reinforced ZrB_2 based ultra high temperature ceramics. *J Eur Ceram Soc* 2023, **43**: 5413–5424.

[37] Zhai WZ, Bai LC, Zhou RH, *et al.* Recent progress on wear-resistant materials: Designs, properties, and applications. *Adv Sci* 2021, **8**: 2003739.

[38] Rodríguez-Rojas F, Zamora V, Guiberteau F, *et al.* Wear of the ultrahard B_4C–SiC–TiB_2 ceramic composite in unlubricated sliding contact with ceramic counter-parts. *J Eur Ceram Soc* 2024, **44**: 5555–5568.

[39] Sciti D, Guicciardi S, Zoli L, *et al.* Dry sliding wear behaviour of ZrB_2-based ceramics: Self-mated and cross coupling with alumina. *J Eur Ceram Soc* 2022, **42**: 6335–6346.

[40] Song JP, Liu SW, Ahmad R, *et al.* Tribological behaviour of TiB_2–HfC ceramic tool material under dry sliding condition. *Ceram Int* 2020, **46**: 20320–20327.

[41] Paul TR, Mondal MK, Mallik M. Abrasive wear performance and wear map of ZrB_2–$MoSi_2$–SiC_w composites. *J Eur Ceram Soc* 2021, **41**: 3227–3251.

[42] Zhang JH, Zheng XW, Liu JX, *et al.* Tribological and wear-resistant behaviors of single-phase $(Dy_{0.2}Ho_{0.2}Er_{0.2}Tm_{0.2}Lu_{0.2})B_{12}$ high-entropy ceramic. *J Eur Ceram Soc* 2024, **44**: 3664–3674.

[43] Sun D, Zhu LS, Cai YC, *et al.* Tribology comparison of laser-cladded CrMnFeCoNi coatings reinforced by three types of ceramic (TiC/NbC/B_4C). *Surf Coat Tech* 2022, **450**: 129013.